JBC RESEARCH ARTICLE

Structural characterization and functional insights into the type II secretion system of the poly-extremophile *Deinococcus radiodurans*

Received for publication, October 5, 2023, and in revised form, November 7, 2023 Published, Papers in Press, December 10, 2023,
https://doi.org/10.1016/j.jbc.2023.105537

Domenica Farci[1,2,3,*], **Stefan Milenkovic**[4], **Luca Iesu**[2], **Marta Tanas**[2], **Matteo Ceccarelli**[4], **and Dario Piano**[1,2,3,*]

From the [1]*Department of Plant Physiology, Warsaw University of Life Sciences - SGGW, Warsaw, Poland;* [2]*Department of Life and Environmental Sciences, Università degli Studi di Cagliari, Cagliari, Italy;* [3]*R&D Department, ReGenFix Laboratories, Sardara, Italy;* [4]*Department of Physics and IOM/CNR, Università degli Studi di Cagliari, Monserrato, Italy*

Reviewed by members of the JBC Editorial Board. Edited by Phillip A. Cole

The extremophile bacterium *D. radiodurans* boasts a distinctive cell envelope characterized by the regular arrangement of three protein complexes. Among these, the Type II Secretion System (T2SS) stands out as a pivotal structural component. We used cryo-electron microscopy to reveal unique features, such as an unconventional protein belt (DR_1364) around the main secretin (GspD), and a cap (DR_0940) found to be a separated subunit rather than integrated with GspD. Furthermore, a novel region at the N-terminus of the GspD constitutes an additional second gate, supplementing the one typically found in the outer membrane region. This T2SS was found to contribute to envelope integrity, while also playing a role in nucleic acid and nutrient trafficking. Studies on intact cell envelopes show a consistent T2SS structure repetition, highlighting its significance within the cellular framework.

Deinococcus radiodurans is a non-motile extremophile known for its remarkable resistance to harsh conditions. Its cell envelope comprises three protein complexes (1), including the S-layer Deinoxanthin Binding Complex (SDBC), a porin that displays superoxide dismutase activity (2–9), the Radial Dimeric (RD) complex (1, 10), that still remains uncharacterized, and a Type II Secretion System (T2SS). The T2SS is evenly distributed in the cell envelope of this bacterium, surrounded by SDBC and RD copies in a structured pattern characteristic for its regularity (1, 10).

T2SSs are part of a large superfamily of Type IV filament-containing systems that share homologous components, including pili and flagella (Type IV Piliation systems, T4P) (11, 12). They are equally spread among Archaea and Bacteria, and a general function of substance secretion as well as DNA uptake related to competence has been assigned (13–18).

Usually, in T2SSs, several regions can be identified (13–18): I) the outer membrane region, an outer membrane-embedded core that consists of the main secretin channel (*e.g.*, GspD or PulD, depending on the nomenclature); II) the pilotin region, a homo-oligomeric belt of an accessory pilotin (*e.g.*, GspS, AspS, or PulS, depending on the nomenclature) localized in the periplasm and facing the Outer Membrane (OM) leaflet; III) the assembly platform, composed of several subunits (*e.g.*, PulC, PulE, PulL, PulM, PulN), localized at the underlying Periplasmic/Peptidoglycan Region and extending into the Inner Membrane (IM); IV) the pseudopilus extrusion machinery, consisting of a helical filament that propels fully-folded substrates through the secretin channel. While various T2SS structures have been previously reported, the distinctive characteristics of the system elucidated in this study add significant value to the growing demand for comprehensive functional and structural data on secretion systems, including T2SSs.

Here, the T2SS, isolated from the wild-type strain R1 of *D. radiodurans*, is structurally described at near-atomic resolution. This case is notable due to the distinctive networking context of this machinery within its highly structured S-layer/cell envelope (1, 10). Two previously uncharacterized lipoprotein subunits, DR_0940 (GspT) and DR_1364 (GspP), play significant roles. DR_0940 forms the T2SS cap, typically a domain of GspD, while DR_1364 forms a belt around the GspD β-barrel region, differing from the usual pilot in S subunits (GspS/PulS/AspS).

Additionally, a novel region named Inner Membrane-Related Region (IMRR) at the base of the complex contributes to a second gate in GspD, supplementing the typical one at the β-barrel region. The T2SS is not only involved in natural competence (19) but, as shown here, also impacts the statics of the cell envelope and its trafficking. Considering the singular networking background of this molecular machine, which is integrated into its much more structured and organized cell envelope/S-layer functional unit, these novel modular and architectural features might have implications for cell envelope/S-layer maintenance. Subtomogram averaging and cryo-electron crystallography on intact cell envelope patches reveal a T2SS repetition with a typical p6 symmetry, consistent with that observed in the S-layer of this bacterium (20). Overall, this T2SS has distinctive features expected to be crucial in shaping the organized structure and functional properties of this cell envelope. A T2SS integrated into such an articulated supramolecular organization could be involved in specialized

* For correspondence: Domenica Farci, domenica.farci@unica.it; Dario Piano, dario.piano@unica.it.

functions characterizing this cell envelope, most of which in this bacterium are aimed at ensuring protection at many levels (*e.g.*, robust cell envelope structures, shielding incoming radiation, quenching oxidative damage). During evolution, similar cases can be expected for many other S-layer-carrying bacteria including pathogens, where the presence of a highly repeated number of T2SS copies in a highly structured cell envelope can be relevant to understand pathogenic mechanisms and may turn out to be useful to develop therapies against new targets. The reported findings and their associated implications contribute to enhancing the overall understanding of Type II Secretion Systems, particularly in species, characterized by highly structured cell envelopes in which these complexes are integrated. This research holds significant potential for technological and biomedical applications.

Results

Structure of the T2SS core

The T2SS from *D. radiodurans* R1 was isolated and resolved at ∼2 Å, revealing a complex structure spanning ∼173 Å in width at its widest point and ∼350 Å in height, in line with the reported cell envelope thickness (1, 21–23) (Figs. 1 and S1). The core is composed by the secretin DR_0774, a pentadecameric GspD, spanning the outer membrane and extending into the periplasm/peptidoglycan, facing the inner membrane (Figs. 1, S1*B*, and S2*A*). The GspD Outer Membrane Region (OMR; residues range 504–740) features a dominant 60 β-sheets β-barrel structure (∼85 Å tall, ∼106 Å internal diameter) (Figs. 1 and 2*A*). For each secretin monomer, two protrusions emerge: the External Upper Protrusion (EUP) in the OM (residues 703–718) and the more extensive External Bottom Protrusion (EBP) in the periplasm (residues 635–645 and 680–690) (Fig. 2*A*). Internally, a Beta Hairpin Motif (BHM, residues 608–629) constricts the channel, creating a periplasmic gate (∼26 Å diameter) (Fig. 2). Below the OMR, the Periplasmic Region (PR; residues 503–156) contains the canonical N domains, N3, N2, N1, and N0 (Fig. 2*A*). Directly beneath the periplasmic gate, a subtly discernible constriction (∼67 Å diameter) related to the N3 domain is visible (Fig. 2*A*). Another constriction at the N0 domain (∼77 Å diameter) connects with the N-terminal part of GspD, the IMRR (Inner

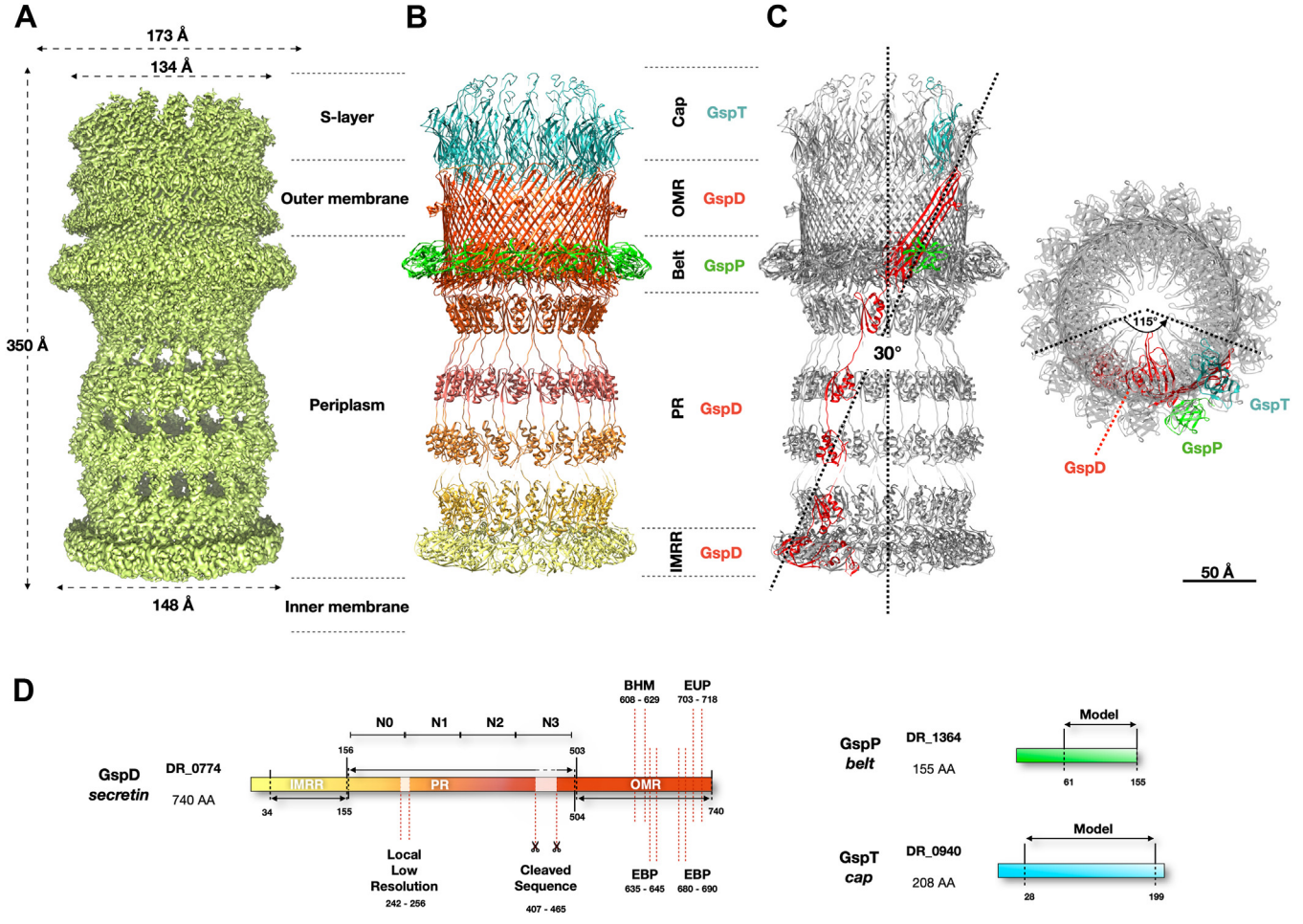

Figure 1. The T2SS structure of *D. radiodurans*. *A*, T2SS cryo-EM map showing the main external dimensions. *B*, T2SS model, a pentadecameric hetero-oligomer, consisting of three different subunits. GspD (DR_0774), in *orange/yellow*, forms the core divided into the Outer Membrane Region (OMR), Periplasmic Region (PR), and Inner Membrane-Related Region (IMRR). GspT (DR_0940), in *light blue*, forms the cap region toward the S-layer. GspP (DR_1364), in *light green*, forms the belt at the outer membrane-periplasm interface. *C*, a GspD monomer (in *red*) tilts ∼30° longitudinally and has ∼115° transversal torsion from the top view (*dashed lines*). Scale bar is 50 Å. *D*, a scheme of GspD (DR_0774) indicates domains, cleaved sequences, and the local low-resolution part. For GspP (DR_1364) and GspT (DR_0940), modeled regions are indicated.

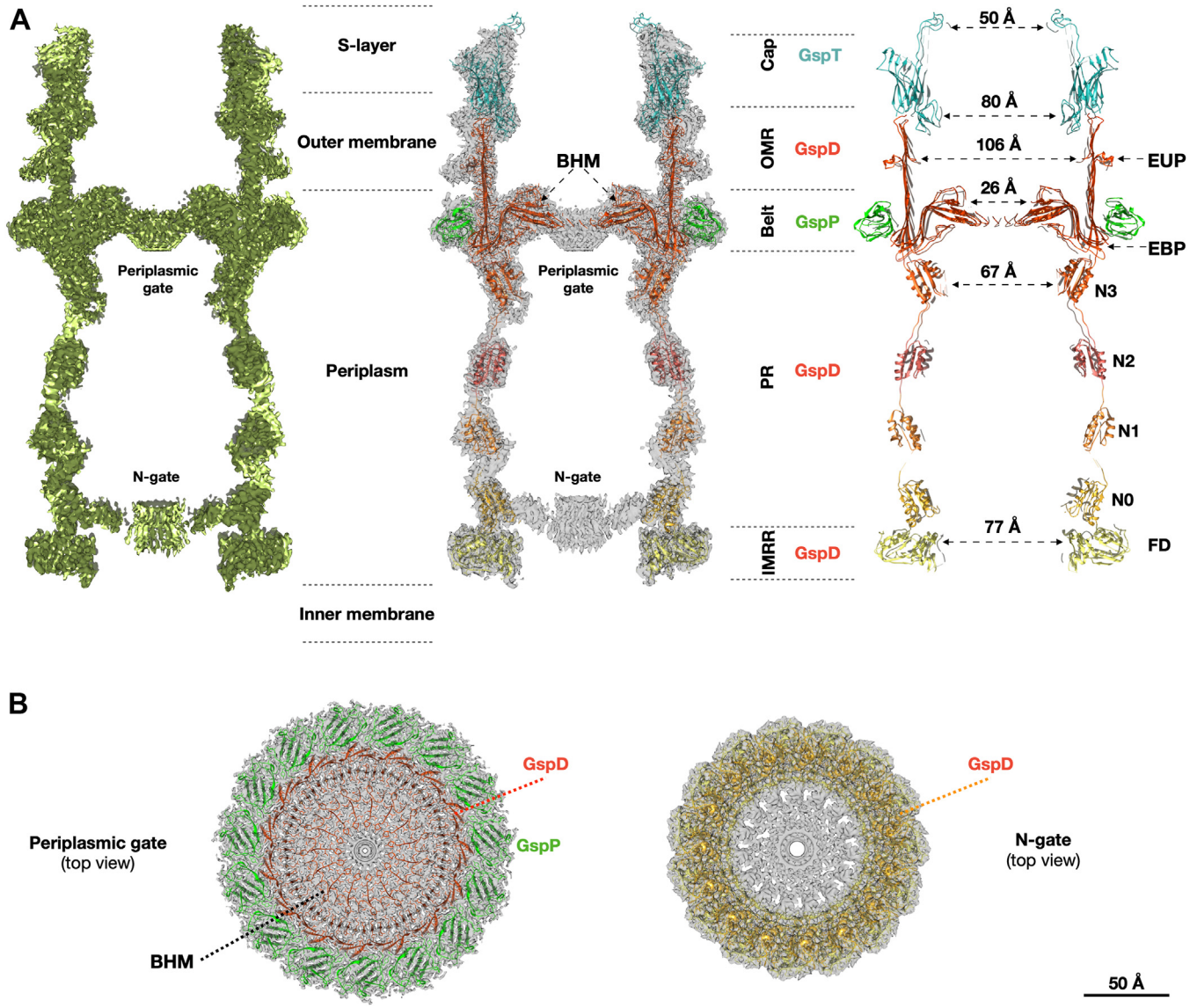

Figure 2. Cross-sections and fitting of the T2SS. *A*, *left* to *right*: T2SS cryo-EM map cross-section, model fitting, and model itself. *Orange/yellow* marks GspD domains: External Upper Protrusion (EUP), External Bottom Protrusions (EBP), N domains (N3 to N0), and the Flange Domain (FD). Internal pore dimensions, gates, and constrictions are also indicated. *B*, images show top-view cross-sections of the maps fitted with the model at the periplasmic (*left*) and the N-gates (*right*) heights. GspD (*orange/yellow*) and GspP (*green*) subunits at these levels are indicated. Scale bar is 50 Å.

Membrane-Related Region, residues range 155–34), and identifies the N-domain-related gate (N-gate; Figs. 2, S2*A*, and S3). The GspD-IMRR is found to be peripheral to the inner membrane (∼1 Å thickness by PPM3.0; Fig. S2*A*), featuring an external diameter of ∼148 Å (Fig. 1) and an internal one of ∼77 Å (Fig. 2*A*). Because of the IMRR's flange shape, likely important to increase the surface of interaction with an inner membrane machinery, we named this newly identified GspD domain as Flange Domain (FD), which appears shorter but larger with respect to the N domains. The secretin DR_0774 was modelled from residue 34 (peripheral to the inner membrane) to residue 740 (outer membrane), with a 59-amino acids gap in the N3 domain and a 15-amino acids gap between the N0 and N1 domains due to a local low resolution of the map (Figs. 1*D* and S1*E*). Each secretin monomer tilts ∼30° along the z-axis and twists ∼115° counterclockwise from the N-terminal to the C-terminal (Fig. 1*C*). Initially classified as a PilQ, the resulting DR_0774 complex was cautiously designed as Type IV-like piliation system (T4P-like), suggesting a potential reclassification pending further data (24). Through structural, phylogenetic, and sequence alignment analyses, this work identifies it as a T2SS, assigning DR_0774 as a GspD (Figs. 3 and S4). The absence of pili in *D. radiodurans* (22) further supports this conclusion.

A pentadecameric ring surrounds the base of the OMR

T2SSs typically feature a pilotin belt (PulS, GspS, or AspS) surrounding GspD. In this case, a 15-fold symmetry belt surrounds the T2SS at the OMR base (Fig. 1). This arrangement relies on electrostatic interactions between belt subunits and the GspD monomers at the EBP level (Figs 2*A*

and S5, *A* and *B*). The belt's monomer, DR_1364, a 155-residues globular protein, has been modelled for 95 amino acids (residues 61–155; Fig. S5). The DR_1364, a predicted IPT/TIG domain-containing protein (Immunoglobulin (Ig)-like fold), lacks homology and folding analogy (β-sheets *versus* α-helices) to known pilotins in others T2SSs (Figs. S4*A*, and S5*C*). This diversity stems from the GspD in this T2SS lacking the common S domain (Fig. 3*C*) that usually interacts with the pilotin S belt (25). Instead, the new belt subunit DR_1364 is secured by the EBP. Considering the uniqueness of this subunit, we here named it GspP, adhering to the T2SS subunits nomenclature. Bioinformatic analysis confirms GspP lipoprotein features with a cleavage site at position 51 to 52 (c-region/site) preceded by a positively charged signal region (n-region; residues 1–37) and a hydrophobic region (h-region; residues 38–51) (Fig. S5*C*). The h-region neighbours the cysteine in position 52 which is deputed to N-lipidation. The range of residues 52 to 61, while present and directed to the OM (GspP OM-link in Fig. S2*A*), could not be modeled.

An independent subunit builds the T2SS cap

The cap domain, found on top of the OMR and only for some species, is usually made of the C-terminal region of the secretin (6) (Fig. S4*A*). In *D. radiodurans,* the T2SS cap domain is made up of an independent subunit that robustly interacts with GspD monomers and with an extended apical part pointing upward (Figs. 1, 2, and S6, *A* and *B*). Notably, a cluster of aromatic residues marks the boundary between GspD and the cap (Fig. S6*A*). This subunit also follows a 15-fold symmetry, giving to the cap its characteristic shape (Figs. 1 and 2). Compared to similar structures, this cap is steeper and narrower, likely enhancing interactions with the outer membrane's structural network (Figs. S2*A* and S4*A*). The cap forms an internal constriction (∼80 Å diameter) at the GspD OMR level and in its uppermost part resolves into an external pore with an internal diameter of ∼50 Å, finally restricting the access to the whole complex (Fig. 2*A*). The cap subunit, identified as the DR_0940, is a 208-residues protein modelled from residue 28 to residue 199 (Figs. 1*D* and S6).

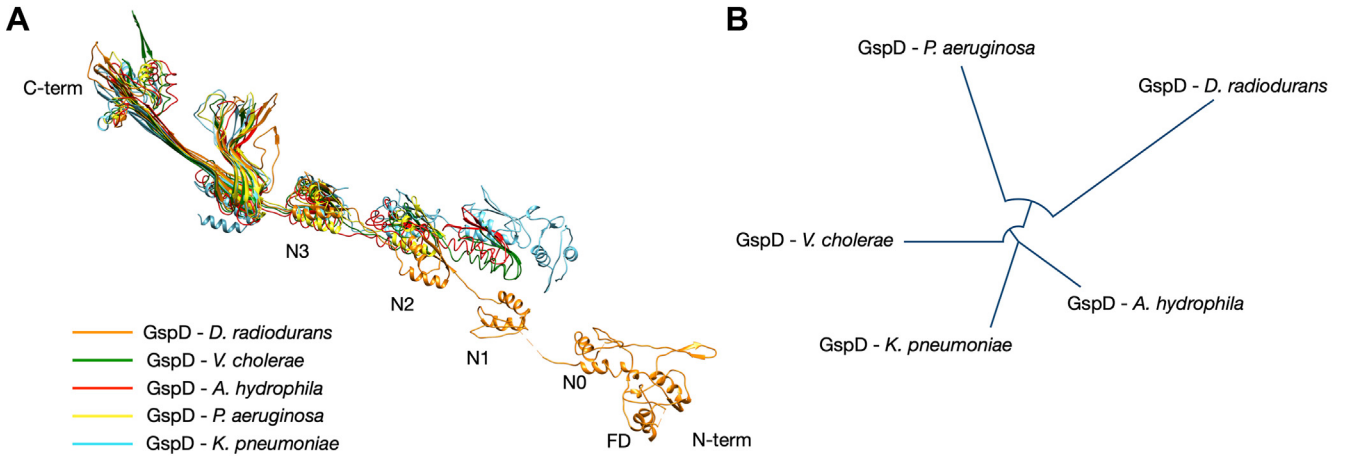

C

Figure 3. GspD phylogenetic and structural comparative analyses. In (*A*), the image presents a comparison of *D. radiodurans* GspD with others GspDs for which the atomic model is available. The analysis indicates structural similarities for the β-barrel region and the first 2 N domains while highlighting an increasing difference going towards the N-terminal part, which ends with the Flange Domain (FD), characteristic of the *D. radiodurans* GspD. The shown GspD are from *D. radiodurans* (8CO1), *K. pneumoniae* (6HCG), *V. cholerae* (5WQ8), *A. hydrophila* (6I1X), and *P. aeruginosa* (5WLN). The color legend is reported in the image. In (*B*), the image shows the phylogenetic tree of the same GspDs reported in (*A*). In (*C*), a multiple-sequence alignment of the same GspDs reported in (*A*) and (*B*) shows a good identity between the entries as well the absence of the S-domain (*blue box*) in the C-terminal region of the *D. radiodurans* GspD, confirming the absence of a typical pilotin S forming the belt around the complex.

Given its uniqueness (Fig. S6*C*), we named the DR_0940 as GspT, adhering to the T2SS subunits nomenclature. Being uncharacterised, no specific functional properties have been assigned. GspT is predicted to be a membrane-interacting protein, likely monotopically, facing the extracellular region which in this bacterium is also of S-layer pertinence. Considering the proximity of the OM, we conducted bioinformatic analysis on the primary GspT sequence for potential lipoprotein features. Results revealed a cleavage site at position 19 to 20 (c-region/site) preceded by a positively charged signal region (n-region; residues 1–5) and a hydrophobic region (h-region; residues 6–19) (Fig. S6*C*). The h-region neighbours the cysteine in position 20 which is deputed to N-lipidation (Fig. S6*C*). Based on the above information, it is likely that the cap contributes to the stability of the S-layer assembly bridging it with the OM.

T2SS cell envelope distribution and localization

In *D. radiodurans,* the T2SS is integrated into a highly structured cell envelope (1, 10). Indeed, in this bacterium, the regularity of the S-layer extends into the layers below and the T2SS represents a main statical component of this organization (1, 10). Here, we have studied the T2SS and its architectural details in the larger structural context where it operates. Studies on intact cell envelope patches (Fig. 4*A* and Movie S1) have been independently performed by subtomogram averaging (Fig. 4*B*) and 2D cryo-electron crystallography (cryo-EC, Fig. 4*C*). Results showed the regular repetition of the T2SS and its relative distribution with a p6 symmetry (Fig. 4*D*), which, for the cryo-EC, was subsequently imposed to improve the final resolution (Fig. 4*C*). In this bacterium, the structural unit, consisting of one T2SS, six SDBCs, and six RDs, is repeated delimiting the entire cell body (1, 10). Therefore, the results

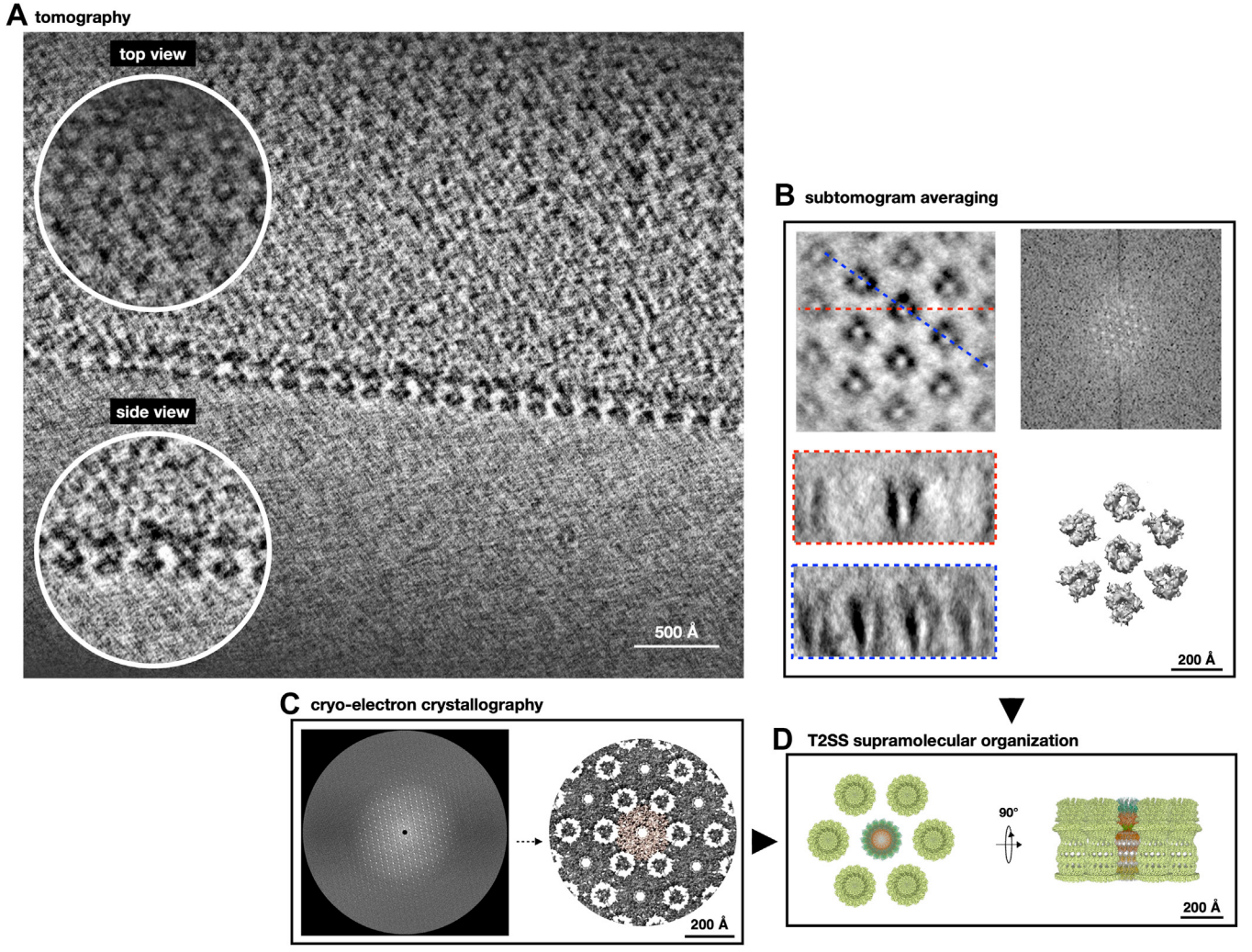

Figure 4. T2SS organization in the cell envelope. *A*, image shows a slice of a tomogram with typical T2SS repetition; zoom-in insets highlight details in top and side views. Scale bar indicates 500 Å. *B*, typical subtomogram averaging: top view (*upper-left* corner) and side views from different angles (*bottom-left* corner); *red-* and *blue-dashed lines* in the top view indicates side-view orientations. FT analysis of tomogram (*upper-right* corner) and the top view of 3D subtomogram averaging volume (*bottom-right* corner) are also shown. *C*, cryo-electron crystallography results: *left*- Fourier coefficients plot from FT analysis of cell envelope patches; *right-top* view of the resulting 3D cryo-EC map with the central T2SSin *orange*. *D*, *top* (*left*) and side (*right*) views scheme illustrating the T2SSs organization in *D. radiodurans* cell envelope. The central T2SS is a map with the model fitted. Scale bars in (*B–D*) indicate 200 Å.

here shown provide a clear overview of the astonishing complexity and regularity characterizing this cell envelope.

The T2SS contributes to cell envelope stability and trafficking

The cell envelope contributes to the trafficking and the poly-extremophile properties of *D. radiodurans* (9, 10, 26, 27). Being highly represented in the cell envelope (1, 10, 24), the T2SS is expected to contribute to its stability. To investigate the functional involvement of the T2SS in the cell envelope and in the extreme resistance of this bacterium, differential effects between the *D. radiodurans* R1 wild type and its DR_0774 deletion mutant were assessed under stress conditions. Either shear stress, with frictional forces, or normal stress, with compression/expansion cycles, were tested by means of mortality post-exposure (Table 1 and Fig. S2*B*). In all cases, the deletion mutant showed to be more sensitive to mechanical stress with respect to the wild type, and with greater sensitivity to normal stress than to the shear one (Table 1 and Fig. S2*B*). In both instances, experiments demonstrate a primary cohesive role associated with the presence of the T2SS.

Considering the role of this S-layer in contributing to the UV-C resistance of *D. radiodurans* R1, we also investigated the potential involvement of the T2SS in resistance against UV-C exposure. Once again, comparative experiments demonstrated increased sensitivity of the deletion mutant in comparison to the wild type (Table 1 and Fig. S2*B*).

Given the cohesive and secretion roles of the T2SS, we examined any disparities in terms of total protein release in the media between the wild type and the mutant. These analyses revealed a six-fold increase in the proteins released in the media for the mutant, highlighting the T2SS's involvement in S-layer stability and integrity (Table 1).

The loss of natural competence in the deletion mutant showed the pivotal role of this secretin and its T2SS in the uptake of nucleic acids (19). Here, the structural information was exploited to perform all-atom molecular dynamics simulations on the T2SS (GspDPT) inserting it in a phospholipid bilayer, either asymmetric with lipopolysaccharides (GspDPT/LPS) or symmetric with phosphatidylcholine (GspDPT/POPC), as usually done in reconstitution experiments (28). As outlined in the Supplementary section, simulations showed the stability of the system in both models. In particular, in the most challenging one, the GspDPT/LPS, along the 300 ns simulations in the Isothermal–isobaric ensemble (NPT), the stability of the LPS's nitrogen and phosphate atoms can be observed (Fig. S7, *A* and *B*). In this model, the Root-Mean-Square-Distance from the initial structure reaches a plateau already after 100 ns, demonstrating the stability of our model (Fig. S7*C*). Similarly, conductance and ion selectivity, in the context of threading of ssDNA or dsDNA 24-mers, were assessed in the simpler GspDPT/POPC model system. Here, the T2SS was found to be prone to ssDNA and dsDNA uptake as well as identified as slightly cation selective (Tables 1 and S2; Fig. S2*C*). These results are in line with other well characterized transport systems of similar size (29, 30).

Discussion

Type II Secretion Systems (T2SS) are molecular assemblies that play a crucial role in cellular trafficking and cell-environment interactions. They are widely distributed in Archaea and Bacteria, including pathogenic species (11–18) and belong to a larger Type IV filament-containing superfamily, alongside pili and flagella (11, 12). In *D. radiodurans*, the core secretin DR_0774 distinguishes itself as a GspD, rather than a PilQ, pointing its assembly to a T2SS more than a T4P. This observation is corroborated by the absence of pili and motility in this bacterium as well as the loss of natural competence in DR_0774 deletion mutants (19). These aspects, coupled with the involvement of two operons in constructing this machinery (Fig. S4*B*; DR_0774 and DR_0940 are part of two different operons), underscore its active functionality within the cellular framework. These findings are further

Table 1
Summary of the functional assays: Comparative analysis of wild type *versus* DR_0774 deletion mutant to assess DR_0774 and its T2SS functionality

					ΔpilQ *versus* WT		
Assayed function	Assay/Prediction		Method	Functional properties	Qualitative (specific property)	Quantitative	Reference
Electromagnetic stress	Spotting pre-exposure	UV-C exposure	Hg lamp (9 W)	UV-C resistance	Decreased	+30.36% (mortality)	this work
Mechanical stress	Spotting post-exposure	Shear exposure	Zirconium-silica beads/Vortexing	Mechanical tethering (spacer)[a]	decreased	+15.25% (mortality)	this work
	Spotting post-exposure	Pressure exposure	French pressure cell/Compression-expansion	Mechanical tethering (spacer)[a]	decreased	+85.40% (mortality)	this work
Cell properties	Electrophoresis	Protein secretion/Cell envelope integrity	Cell growth/ Supernatant analysis	Protein release in the media	increased	~6x	this work
Trafficking	Spotting post-exposure	DNA uptake	pRAD1 plasmid/ Transformation	Natural competence	precluded	0	Ref. (19)
	Molecular dynamics	ssDNA trafficking	Molecular dynamics	Natural competence	n.a.	n.a.	this work
	Molecular dynamics	dsDNA trafficking	Molecular dynamics	Natural competence	n.a.	n.a.	this work
	Molecular dynamics	Ion transport	Molecular dynamics	Nutrient uptakes	n.a.	n.a.	this work

[a] This function is specified to distinguish from the one of mechanical tethering as a turnbuckle for the SDBC[3].

corroborated by the functional tests here reported (Tables 1 and S1; Fig. S2*C* and Movies S2–S4). In *D. radiodurans,* the T2SS is highly repeated and regularly organized through the cell envelope (1, 10). Subtomogram averaging and 2D cryo-EC on large cell envelope fragments further detailed this property.

While some features are in line with those found in other species, particularly the shared structural similarity from the GspD C-terminal side to the N3 domain as well as its pentadecameric assembly (Figs. 3 and S4), this T2SS also presents distinctive features. Notably the typical S domain, important for the pilotin S binding and characterizing the T2SS in *K. pneumoniae* and *E. coli* ETEC (Fig. S4*A*), here is absent (Fig. 3*C*). Consequently, also the pilotin S is here replaced by the unrelated GspP. Interestingly, the pilotin S of these species has typically a structure built by α-helixes, while the GspP structure has a β-barrel organization. The N0 domain exhibits a distinct sequence when compared to other GspDs featuring this domain as exemplified by *K. pneumoniae* complex(Figs. 3*C* and S4*A*). Additionally, the *D. radiodurans* complex displays a greater height (∼350 Å of this T2SS *versus* ∼220 Å; Fig. S4*A*) in comparison to known T2SS systems (12, 17), including the extensively studied counterpart from *K. pneumoniae*. This aspect is likely due to the thicker cell envelope of *D. radiodurans* (1, 21–23) when compared with other systems. This extension is attributed to the presence of GspT as an independent subunit building itself the cap structure, and an additional domain at the N-terminal part of GspD, the FD (Figs. 2, 3*A*, and S4*A*). In the cases of *E. coli ETEC* and *K. pneumoniae,* a cap formed by the C-terminal region of GspD is present, although it is different in shape and less pronounced compared to the cap build in *D. radiodurans* by the GspT, which is more extended and built by an individual subunit. Finally, the FD, a domain exclusive of *D. radiodurans'* GspD lies at the inner membrane's periphery (Fig. S2*A*) and is likely monotopic, thereby enhancing the interaction with specific protein components in the inner membrane (24, 31). The repeated T2SS structure acts as an effective spacer, stabilizing the cell envelope and maintaining cellular integrity. Resistance tests on the DR_0774 deletion mutant further emphasize its importance in withstanding mechanical stress (Table 1).

Finally, although the gate regions inside the channel were not modeled due to a local lower resolution, several details can be appreciated for both, the periplasmic and N- gates, which occur with a typical check-valve organization and are expected to have a primary role in the functionality of the complex (Figs. S2*A* and S3). The specific function of N0 in the N-gate and its difference from the N0 of *K. pneumoniae*, the only one structurally identified to date, could result from specialization, elucidating its divergence from known T2SS systems (Figs. 3*C* and S4*A*). GspT acts as an independent T2SS subunit, forming a cap toward the environment and likely serving as a bridge to the S-layer. In the previously characterized GspDs, the C-terminal part is involved in building the cap. Interestingly, this part nicely fits between GspDs including the one of *D. radiodurans* R1 (Fig. 3*A*) even if, in the latter case, none of the domains are involved in the cap structure (Fig. S4*A*).

The GspP, characterized by its Ig-like fold, contributes to the transversal continuity with the neighboring complexes (1, 10). The presence of such proteins in prokaryotes is associated with cell surface receptors and the inside-out evolution of cells (32–34).

D. radiodurans exhibits a three-dimensionally organized cell envelope with specialized multi-subunit assemblies, including the SDBC and the T2SS (1, 10). This intricate supramolecular organization is a result of deep evolutionary adaptations to ensure protection against various stressors (1–10). Similar mechanisms may be widespread among bacteria, offering insights into their strategies for environmental resilience.

Experimental procedures

Cell culturing, T2SS purification, and identification

D. radiodurans (strain R1; ATCC 13939) was grown in Tryptone Glucose Yeast extract (TGY) at 30 °C for 24 h as described in (24). Cell envelope and T2SS isolation followed previous protocols (1, 10, 24). Samples' quality was assessed by Blue Native (BN) gel electrophoresis, using 3 to 12% (w/v) gradient gels (NativePAGE, Invitrogen) (9). Chromatography columns were regenerated and calibrated prior use by ReGenFix (https://www.regenfix.eu/) (1).

Bioinformatic analysis

SignalP-6.0 (35) (https://services.healthtech.dtu.dk/services/SignalP-6.0) was used for signal peptide and cleavage site prediction. UniProt (36) (https://www.uniprot.org) and DIVEIN (37) (https://indra.mullins.microbiol.washington.edu/DIVEIN/index.htm) aided in multiple-sequence alignment as well as phylogenetic and divergence trees. Operons were predicted using MicrobesOnline (38) (http://www.microbesonline.org/). The transmembrane regions were predicted *via* the PPM 3.0 web server (39) (https://opm.phar.umich.edu/ppm_server).

Cryo-electron microscopy data acquisition

Grids preparation and data acquisition for Either purified T2SS sample (5 mg/ml) or cell envelope fragments were done at CEITEC (Brno, Czech Republic) according to (3). Any minor modification has been reported in Table S3. Supplemental information is provided in the SI and Fig. S8.

Data processing

The data processing for single-particle analysis was done using cryoSPARC (40) according to (3), with the following differences. Any minor modification has been reported in the Supporting information and Table S3. From the obtained and refined map, a *de novo* model was built using Coot software (41). For the three subunits, first the poly-A models were manually built, then, based also on the main subunits identified by MS (24), manually assigned using Coot (41). The final model was refined with the Phenix software (42), while visualization and fittings were done using the Chimera software (43).

The cryo-electron tomography and subtomogram averaging analyses were done with the *etomo* package, *imod* and

PEET software (44–46), according to (1). Any minor modifications and details have been reported in Table S3. The cryo-electron crystallography analyses were done with *2dx* and Focus packages (47, 48) according to (1, 10) with no modification.

Stress assays and effects assessment

Resistance assays involved growing *D. radiodurans* R1 strains WT and ΔDR_0774 in TGY for 24 h at 25 °C (OD_{650} = 1.2) (5, 6). Cell cultures underwent a 10× series of five dilutions (from 10^{-1} to 10^{-5}) with the last four spotted in 3 μl volumes on 1.5% agar TGY plates. Colony Forming Units (CFU) count was performed on the 10^{-3} dilution. Shear and normal stress experiments were performed on culture suspensions by (i) vortexing at 2000 rpm with a 4.5 mm orbital diameter for 30 min with a 1:1 (w/w) ration of 5-mm zirconium-silica beads to cultures; (ii) a french pressure cell at 900 Ψ on 15 ml cultures for two cycles. Spotting was done post-exposure. Electromagnetic stress experiments were performed using a 9 W UVC lamp placed at 15 cm from the plate (irradiation rate of 2.75 J/s/m^2) for 5 min and then incubated for 48 h at 25 °C. Spotting was done pre-exposure. Cell envelope integrity was assessed *via* centrifugation (5000*g*, 10 min, 4 °C) and concentration/dilution in Phosphate buffer 50 mM pH 7.4, 0.05% β-DDM using a 10 kDa cutoff (Vivaspin Turbo 15, Sartorius). Protein differences were estimated by SDS-PAGE and absorption spectroscopy at 280 nm.

Molecular dynamics simulations

The procedure described in (49) (https://www.ks.uiuc.edu/Training/Tutorials - Membrane Protein Tutorials) for membrane-protein system preparation was followed. For both systems, GspDPT/LPS and GspDPT/POPC, the entire procedure was performed using the CHARMM-GUI server (50). The software CHARMM 36 m force field for proteins (51), CHARMM 36 for lipids and DNA (52), TIP3P for water (53), and the new Multi-Site model for Ca^{2+} were used (54–57). The server Propka (58) suggested all amino acids in their standard protonation state at neutral pH. The final systems were simulated on a 20-cores CPU equipped with a single RTX-3090 GPU using Gromacs 2022.4, with a performance of 18 to 21 ns/day. After equilibration and 10 ns in the NPT ensemble, we started the simulations at zero voltage and thus at different voltages (Table S1). Further, we added DNA 24-mers (6A-6C-6G-6T), either ssDNA or dsDNA, placed partially in the pore above and below the filter with the orientation three′ forward (59), as reported in Fig. S2*C* and performed DNA threading simulations.

Quantification and statistical analysis

Cell envelope and T2SS isolations for data analyses were performed on more than 40 independent preparations. All data are representative of at least three independent replicates. All attempts to reproduce the results here presented were successful.

Data availability

Materials, data, and protocols are accessible in the article and public repository Electron Microscopy Data Bank (EMDB) (EMD-16770 and PDB ID-8CO1). Data will be released upon publication. This article does not report any original code.

Supporting information—This article contains supporting information (60–65).

Acknowledgments—We acknowledge the cryo-electron microscopy and tomography core facility CEITEC MU of CIISB. The authors are grateful to: Dr J. Nováček and Mgr. D. Pinkas for the support at the cryo-EM core facility; Dr P. Servant for kindly proving the DR_0774 deletion mutant. We finally thank Miss Maria Bonaria Farci for the kind support with the images.

Author contributions—D. P. and D. F. conceptualization; D. P. and D. F. validation; D. P. and D. F. formal analysis; D. P. and D. F. funding acquisition; D. P. and D. F. project administration; D. P. and D. F. supervision; D. P., D. F., S. M., and M. C. methodology; D. P., D. F., S. M., M. C., L. I., and M. T. investigation. S. M. and M. C. resources; D. P., D. F., S. M., and M. C. visualization; D. P., D. F., S. M., M. C., L. I., and M. T. writing–original draft; D. P., D. F., S. M., M. C., L. I., and M. T. writing–review and editing.

Funding and additional information—This work was supported by the National Science Center (Poland) with the Sonata BIS seven Program (2017) Grant PRO-2017/26/E/NZ1/00344 and the Harmonia 10 Program (2018) Grant PRO-2018/30/M/NZ1/00284 (both to D. P. and D. F.). We acknowledge the Instruct-CZ Centre supported by MEYS CR (LM2018127) and iNEXT-Discovery, project number 871037, funded by the Horizon 2020 program of the European Commission (specific project PID 21601, D. F. and D. P.).

Conflict of interest—The authors declare that they have no conflicts of interest with the contents of this article.

Abbreviations—The abbreviations used are: EBP, External Bottom Protrusion; EUP, External Upper Protrusion; FD, Flange Domain; IMRR, Inner Membrane-Related Region; OMR, Outer Membrane Region; PR, Periplasmic Region; SDBC, S-layer Deinoxanthin Binding Complex; T2SS, Type II Secretion Systems.

References

1. Farci, D., Haniewicz, P., and Piano, D. (2022) The structured organization of *Deinococcus radiodurans*' cell envelope. *Proc. Natl. Acad. Sci. U. S. A.* **119**, e2209111119
2. Farci, D., Haniewicz, P., de Sanctis, D., Iesu, L., Kereïche, S., Winterhalter, M., *et al.* (2022) The cryo-EM structure of the S-layer deinoxanthin-binding complex of *Deinococcus radiodurans* informs properties of its environmental interactions. *J. Biol. Chem.* **298**, 102031
3. Farci, D., Graça, A. T., Iesu, L., de Sanctis, D., and Piano, D. (2023) The SDBC is active in quenching oxidative conditions and bridges the cell envelope layers in *Deinococcus radiodurans*. *J. Biol. Chem.* **299**, 102784
4. Farci, D., Bowler, M. W., Esposito, F., McSweeney, S., Tramontano, E., and Piano, D. (2015) Purification and characterization of DR_2577 (SlpA) a major S-layer protein from *Deinococcus radiodurans*. *Front. Microbiol.* **6**, 414
5. Farci, D., Slavov, C., Tramontano, E., and Piano, D. (2016) The S-layer protein DR_2577 binds deinoxanthin and under desiccation conditions protects against UV-radiation in *Deinococcus radiodurans*. *Front. Microbiol.* **7**, 155

6. Farci, D., Slavov, C., and Piano, D. (2018) Coexisting properties of thermostability and ultraviolet radiation resistance in the main S-layer complex of *Deinococcus radiodurans*. *Photochem. Photobiol. Sci.* **17**, 81–88
7. Farci, D., Guadalupi, G., Bierła, K., Lobinski, R., and Piano, D. (2019) The role of iron and copper on the oligomerization dynamics of DR_2577, the main S-layer protein of *Deinococcus radiodurans*. *Front. Microbiol.* **10**, 1450
8. Adamec, F., Farci, D., Bína, D., Litvín, R., Khan, T., Fuciman, M., *et al.* (2020) Photophysics of deinoxanthin, the keto-carotenoid bound to the main S-layer unit of *Deinococcus radiodurans*. *Photochem. Photobiol. Sci.* **19**, 495–503
9. Farci, D., Aksoyoglu, M. A., Farci, S. F., Bafna, J. A., Bodrenko, I., Ceccarelli, M., *et al.* (2020) Structural insights into the main S-layer unit of *Deinococcus radiodurans* reveal a massive protein complex with porin-like features. *J. Biol. Chem.* **295**, 4224–4236
10. Farci, D., Kereïche, S., Pangeni, S., Haniewicz, P., Bodrenko, I. V., Ceccarelli, M., *et al.* (2021) Structural analysis of the architecture and *in situ* localization of the main S-layer complex in *Deinococcus radiodurans*. *Structure* **29**, 1279–1285.e3
11. Makarova, K. S., Koonin, E. V., and Albers, S. V. (2016) Diversity and evolution of type IV pili systems in Archaea. *Front. Microbiol.* **7**, 667
12. Naskar, S., Hohl, M., Tassinari, M., and Low, H. H. (2021) The structure and mechanism of the bacterial type II secretion system. *Mol. Microbiol.* **115**, 412–424
13. Jyot, J., Balloy, V., Jouvion, G., Verma, A., Touqui, L., Huerre, M., *et al.* (2011) Type II secretion system of *Pseudomonas aeruginosa*: *in vivo* evidence of a significant role in death due to lung infection. *J. Infect. Dis.* **203**, 1369–1377
14. Johnson, T. L., Waack, U., Smith, S., Mobley, H., and Sandkvist, M. (2015) *Acinetobacter baumannii* is dependent on the type II secretion system and its substrate LipA for lipid utilization and *in vivo* fitness. *J. Bacteriol.* **198**, 711–719
15. Cianciotto, N. P., and White, R. C. (2017) Expanding role of type II secretion in bacterial pathogenesis and beyond. *Infect. Immun.* **85**, e00014-17
16. Elhosseiny, N. M., and Attia, A. S. (2018) *Acinetobacter*: an emerging pathogen with a versatile secretome. *Emerg. Microbes Infect.* **7**, 33
17. Chernyatina, A. A., and Low, H. H. (2019) Core architecture of a bacterial type II secretion system. *Nat. Commun.* **10**, 5437
18. López-Castilla, A., Thomassin, J. L., Bardiaux, B., Zheng, W., Nivaskumar, M., Yu, X., *et al.* (2017) Structure of the calcium-dependent type 2 secretion pseudopilus. *Nat. Microbiol.* **2**, 1686–1695
19. Ithurbide, S., Coste, G., Lisboa, J., Eugénie, N., Bentchikou, E., Bouthier de la Tour, C., *et al.* (2020) Natural transformation in *Deinococcus radiodurans*: a genetic analysis reveals the major roles of DprA, DdrB, RecA, RecF, and RecO proteins. *Front. Microbiol.* **11**, 1253
20. Baumeister, W., Barth, M., Hegerl, R., Guckenberger, R., Hahn, M., and Saxton, W. O. (1986) Three-dimensional structure of the regular surface layer (HPI layer) of *Deinococcus radiodurans*. *J. Mol. Biol.* **187**, 241–250
21. Murray, R. G. E. (1992) The Family *Deinococcaceae*. In: Balows, A., Trüper, H. G., Dworkin, M., Harder, W., Schleifer, K. H., eds. *The Prokaryotes*, Springer, New York, NY: 3732–3744
22. Rothfuss, H., Lara, J. C., Schmid, A. K., and Lidstrom, M. E. (2006) Involvement of the S-layer proteins Hpi and SlpA in the maintenance of cell envelope integrity in *Deinococcus radiodurans* R1. *Microbiology (Reading)* **152**, 2779–2787
23. Work, E., and Griffiths, H. (1968) Morphology and chemistry of cell walls of *Micrococcus radiodurans*. *J. Bacteriol.* **95**, 641–657
24. Farci, D., Bowler, M. W., Kirkpatrick, J., McSweeney, S., Tramontano, E., and Piano, D. (2014) New features of the cell wall of the radio-resistant bacterium *Deinococcus radiodurans*. *Biochim. Biophys. Acta* **1838**, 1978–1984
25. Nickerson, N. N., Tosi, T., Dessen, A., Baron, B., Raynal, B., England, P., *et al.* (2011) Outer membrane targeting of secretin PulD protein relies on disordered domain recognition by a dedicated chaperone. *J. Biol. Chem.* **286**, 38833–38843
26. Cox, M. M., and Battista, J. R. (2005) Deinococcus radiodurans - the consummate survivor. *Nat. Rev. Microbiol.* **3**, 882–892
27. Richmond, R. C., Sridhar, R. P., Zhou, Y., and Daly, M. J. (1999) Physicochemical survival pattern for the radiophile D. radiodurans: a polyextremophile model for life on Mars. *SPIE Opt. Photon.* **3755**, 210–222
28. Gutsmann, T., Heimburg, T., Keyser, U., Mahendran, K. R., and Winterhalter, M. (2015) Protein reconstitution into freestanding planar lipid membranes for electrophysiological characterization. *Nat. Protoc.* **10**, 188–198
29. Bonome, E. L., Cecconi, F., and Chinappi, M. (2017) Electroosmotic flow through an α-hemolysin nanopore. *Microfluid. Nanofluidics* **21**, 96
30. Mayer, S. F., Cao, C., and Dal Peraro, M. (2022) Biological nanopores for single-molecule sensing. *iScience* **25**, 104145
31. Kota, S., and Misra, H. S. (2008) Identification of a DNA processing complex from *Deinococcus radiodurans*. *Biochem. Cell Biol.* **86**, 448–458
32. Baranova, E., Fronzes, R., Garcia-Pino, A., Van Gerven, N., Papapostolou, D., Péhau-Arnaudet, G., *et al.* (2012) SbsB structure and lattice reconstruction unveil Ca2+ triggered S-layer assembly. *Nature* **487**, 119–122
33. von Kügelgen, A., Alva, V., and Bharat, T. A. M. (2021) Complete atomic structure of a native archaeal cell surface. *Cell Rep.* **37**, 110052
34. Baum, D. A., and Baum, B. (2014) An inside-out origin for the eukaryotic cell. *BMC Biol.* **12**, 76
35. Teufel, F., Almagro Armenteros, J. J., Johansen, A. R., Gíslason, M. H., Pihl, S. I., Tsirigos, K. D., *et al.* (2022) SignalP 6.0 predicts all five types of signal peptides using protein language models. *Nat. Biotechnol.* **40**, 1023–1025
36. UniProt Consortium (2023) UniProt: the universal protein knowledgebase in 2023. *Nucleic Acids Res.* **51**, D523–D531
37. Deng, W., Maust, B. S., Nickle, D. C., Learn, G. H., Liu, Y., Heath, L., *et al.* (2019) DIVEIN: a web server to analyze phylogenies, sequence divergence, diversity, and informative sites. *Biotechniques* **48**, 405–408
38. Dehal, P. S., Joachimiak, M. P., Price, M. N., Bates, J. T., Baumohl, J. K., Chivian, D., *et al.* (2010) MicrobesOnline: an integrated portal for comparative and functional genomics. *Nucleic Acids Res.* **38**, D396–400
39. Lomize, A. L., Todd, S. C., and Pogozheva, I. D. (2022) Spatial arrangement of proteins in planar and curved membranes by PPM 3.0. *Protein Sci.* **31**, 209–220
40. Punjani, A., Rubinstein, J. L., Fleet, D. J., and Brubaker, M. A. (2017) cryoSPARC: algorithms for rapid unsupervised cryo-EM structure determination. *Nat. Methods* **14**, 290–296
41. Emsley, P., and Cowtan, K. (2004) Coot: model-building tools for molecular graphics. *Acta Crystallogr.* **D60**, 2126–2132
42. Liebschner, D., Afonine, P. V., Baker, M. L., Bunkóczi, G., Chen, V. B., Croll, T. I., *et al.* (2019) Macromolecular structure determination using X-rays, neutrons and electrons: recent developments in Phenix. *Acta Crystallogr. D Struct. Biol.* **75**, 861–877
43. Pettersen, E. F., Goddard, T. D., Huang, C. C., Couch, G. S., Greenblatt, D. M., Meng, E. C., *et al.* (2004) UCSF Chimera—a visualization system for exploratory research and analysis. *J. Comput. Chem.* **25**, 1605–1612
44. Kremer, J. R., Mastronarde, D. N., and McIntosh, J. R. (1996) Computer visualization of three-dimensional image data using IMOD. *J. Struct. Biol.* **116**, 71–76
45. Cope, J., Heumann, J. M., and Hoenger, A. (2011) Cryo-electron tomography for structural characterization of macromolecular complexes. *Curr. Protoc. Protein Sci.* https://doi.org/10.1002/0471140864.ps1713s65
46. Heumann, J. M., Hoenger, A., and Mastronarde, D. N. (2011) Clustering and variance maps for cryo-electron tomography using wedge-masked differences. *J. Struct. Biol.* **175**, 288–299
47. Gipson, B., Zeng, X., Zhang, Z. Y., and Stahlberg, H. (2007) 2dx—user-friendly image processing for 2D crystals. *J. Struct. Biol.* **157**, 64–72
48. Biyani, N., Righetto, R. D., McLeod, R., Caujolle-Bert, D., Castano-Diez, D., Goldie, K. N., *et al.* (2017) The interface between data collection and data processing in cryo-EM. *J. Struct. Biol.* **198**, 124–133
49. Li, Y., Liu, J., and Gumbart, J. C. (2021) Preparing membrane proteins for simulation using CHARMM-GUI. *Methods Mol. Biol.* **2302**, 237–251
50. Lee, J., Cheng, X., Swails, J. M., Yeom, M. S., Eastman, P. K., Lemkul, J. A., *et al.* (2016) CHARMM-GUI input generator for NAMD, GROMACS, AMBER, OpenMM, and CHARMM/OpenMM simulations using the CHARMM36 additive force field. *J. Chem. Theor. Comput.* **12**, 405–413

51. Huang, J., Rauscher, S., Nawrocki, G., Ran, T., Feig, M., de Groot, B. L., *et al.* (2017) CHARMM36m: an improved force field for folded and intrinsically disordered proteins. *Nat. Methods* **14**, 71–73
52. Hart, K., Foloppe, N., Baker, C. M., Denning, E. J., Nilsson, L., and Mackerell, A. D., Jr. (2012) Optimization of the CHARMM additive force field for DNA: improved treatment of the BI/BII conformational equilibrium. *J. Chem. Theor. Comput.* **8**, 348–362
53. Klauda, J. B., Venable, R. M., Freites, J. A., O'Connor, J. W., Tobias, D. J., Mondragon-Ramirez, C., *et al.* (2010) Update of the CHARMM all-atom additive force field for lipids: validation on six lipid types. *J. Phys. Chem. B* **114**, 7830–7843
54. Zhang, A., Yu, H., Liu, C., and Song, C. (2020) The Ca^{2+} permeation mechanism of the ryanodine receptor revealed by a multi-site ion model. *Nat. Commun.* **11**, 922
55. Ives, C. M., Thomson, N. J., and Zachariae, U. (2023) A cooperative knock-on mechanism underpins Ca^{2+}-selective cation permeation in TRPV channels. *J. Gen. Physiol.* **155**, e202213226
56. Schackert, F. K., Biedermann, J., Abdolvand, S., Minniberger, S., Song, C., Plested, A. J. R., *et al.* (2023) Mechanism of calcium permeation in a glutamate receptor ion channel. *J. Chem. Inf. Model.* **63**, 1293–1300
57. Liu, C., Zhang, A., Yan, N., and Song, C. (2021) Atomistic details of charge/space competition in the Ca^{2+} selectivity of ryanodine receptors. *J. Phys. Chem. Lett.* **12**, 4286–4291
58. Li, H., Robertson, A. D., and Jensen, J. H. (2005) Very fast empirical prediction and rationalization of protein pKa values. *Proteins* **61**, 704–721
59. Mathé, J., Aksimentiev, A., Nelson, D. R., Schulten, K., and Meller, A. (2005) Orientation discrimination of single-stranded DNA inside the alpha-hemolysin membrane channel. *Proc. Natl. Acad. Sci. U. S. A.* **102**, 12377–12382
60. Mastronarde, D. N. (2005) Automated electron microscope tomography using robust prediction of specimen movements. *J. Struct. Biol.* **152**, 36–51
61. Zheng, S. Q., Palovcak, E., Armache, J. P., Verba, K. A., Cheng, Y., and Agard, D. A. (2017) MotionCor2: anisotropic correction of beam-induced motion for improved cryo-electron microscopy. *Nat. Methods* **14**, 331–332
62. Zhang, K. (2016) Gctf: Real-time CTF determination and correction. *J. Struct. Biol.* **193**, 1–12
63. Ludtke, S. J., Baldwin, P. R., and Chiu, W. (1999) EMAN: semiautomated software for high-resolution single-particle reconstructions. *J. Struct. Biol.* **128**, 82–97
64. Wagner, T., Merino, F., Stabrin, M., Moriya, T., Antoni, C., Apelbaum, A., *et al.* (2019) SPHIRE-crYOLO is a fast and accurate fully automated particle picker for cryo-EM. *Commun. Biol.* **2**, 218
65. Scheres, S. H. (2012) RELION: implementation of a Bayesian approach to cryo-EM structure determination. *J. Struct. Biol.* **180**, 519–530